A Prepulsing Technique for the Characterization of GaN Power Amplifiers With Dynamic Supply Under Controlled Thermal and Trapping States

Corrado Florian, *Member, IEEE*, Tommaso Cappello, *Member, IEEE*, Alberto Santarelli, *Member, IEEE*, Daniel Niessen, *Member, IEEE*, Fabio Filicori, and Zoya Popović, *Fellow, IEEE*

Abstract—The asymmetry between capture and release time constants associated with charge-trapping phenomena observed in the electrical characteristics of microwave gallium–nitride (GaN) field-effect transistors (FETs) introduces distortion in GaN-based power amplifiers (PA). The PAs that operate with supply modulation to increase efficiency are particularly affected by this phenomenon, since the GaN FET trap state exhibits a nonlinear dependence on the voltage applied to the device terminals. In this paper, a measurement approach and the setup are presented for a large-signal characterization of GaN-based PAs operated with dynamic bias supply: a new prepulsing technique is introduced, which enables the characterization of the PA in controlled charge-trapping and thermal states. The characteristics obtained with this technique are shown to give an accurate description of the PA performance in the actual application working conditions. The proposed approach is validated by using the measured data for the direct computation of predistortion functions for the linearization of a 9.7-GHz envelope tracking 10-W GaN monolithic microwave integrated circuit PA for amplitude-modulated pulsed radar transmitters. Additional research on the PA trap-induced performance degradation is also presented and can be explored to predict the PA performance for different parameters of the operative regime or for the formulation of the PA behavioral models.

Index Terms—Amplifier measurements, envelope tracking (ET), gallium nitride (GaN), pulsed measurement, radar pulse shaping, supply modulation, trapping effects.

I. INTRODUCTION

THE electrical performance of gallium–nitride (GaN)-based high-electron-mobility transistors (HEMTs) for microwave applications is affected by charge-trapping mechanisms documented in the literature (see [1]–[5]), such as current collapse and knee walkout in the device pulsed I/V characteristics. These phenomena have an impact on power amplifier (PA) design, and are typically responsible for reduced output power density and power-added efficiency at increasing drain voltages (see [6]–[9]). Indeed, while for

technologies not affected by traps, as GaAs HEMT (almost trap-free nowadays) and silicon LDMOS, an increase of the drain supply voltage typically results, with the appropriate design and thermal management, in the expected increase of the output power (P_{out} is typically proportional to V_D^α with $\alpha = 1.5$–2 depending on the PA class), GaN-on-SiC processes usually deliver less-than-expected output power at increasing drain voltage bias, due to the trap-assisted degradation of the HEMT transconductance that becomes really significant at high-voltage levels. Therefore, the suggested maximum drain voltage bias for such technologies is often not limited by the breakdown of the device or by the thermal constrains, but by the fact that exceeding a certain drain voltage level does not provide substantial increment in output power due to the strong trapping mechanisms, compared to the increased device stress and corresponding degraded reliability [i.e., mean time before failure], due to high fields associated with augmented voltages.

In addition to output power and efficiency degradation, the trap-assisted phenomena can also cause distortion of the PA output signal. This may happen for instance when dealing with repetitive pulse patterns featuring temporizations comparable with typical time constants of charge trap captures and releases, such as in the case of radar sequences containing long silence durations between successive bursts of RF pulses. As described in [10], the pulse-to-pulse stability of a radar pattern, degraded by the trap-assisted or thermal-related low-frequency dispersion, can be improved with the introduction of a warm-up supply gate pulse before each RF pulse within the radar burst. A reproducible quasi-steady-state working regime is obtained, which improves the stability of the performance only at the expenses of a slightly reduced efficiency.

As shown in [1]–[5], time constants associated with charge-trapping effects in GaN FETs show a substantial asymmetry between charge capture (very fast, in the order of picoseconds) and release (up to several seconds). Moreover, it has been observed that the trap state is mainly[1] set by the instantaneous peak values of the voltages applied to the device terminals with nonlinear dependence (maximum peaks of drain voltages and negative peaks of gate voltages). Device models specific to GaN HEMTs have been proposed to describe such

---

[1]The trap state can also exhibit a more complex dependency on voltages, especially when below-threshold operation is involved [9]. This will be also briefly discussed in Section II.

behavior (see [11]–[14]). When dealing with GaN FETs modeling, special attention should be paid to characterize the device by maintaining not only a fixed thermal state, but also a constant trapped-charge state. For instance, this is achieved by means of sinusoidal excitations at low frequencies, as in [14], or this can be obtained through pulsed measurements, as in [13]. In this case, the measurement setup for pulsed I/V characterization was suitably modified with respect to conventional instrumentation to account for trapping mechanisms under isothermal and isodynamic (i.e., isotrap) conditions.

In particular, the double-pulse I/V technique described in [2] works by applying very fast (a few tens of ns) prepulses (PP) toward a selected voltage pair $V_{G,PP}$, $V_{D,PP}$ immediately before each set of measure pulses (with duration similar to PP) toward $V_{G,MP}$, $V_{D,MP}$ (with $V_{G,MP} \geq V_{G,PP}$ and $V_{D,MP} \leq V_{D,PP}$), where the acquisition of a sample of the I/V characteristic is carried out. These very fast PP lead the FET to operate at a gate voltage $V_{G,PP}$ and at a drain voltage $V_{D,PP}$, where a fixed (and maximum) amount of charge is trapped due to the very fast capture times involved (in the order of picoseconds) [2]. Since the release of trap charges occur, instead, in much longer times (in the order of ms), the acquisition of each I/V sample may be conveniently carried out during all the measure pulses without modification of the total amount of trapped charge set by the PP. By indicating with X an equivalent trap-state variable, somehow related to the amount of trapped charge into the FET and nonlinearly depending on $V_{G,PP}$, $V_{D,PP}$, then X reaches a maximum value X_{MAX} ($X = X_{MAX}$) when $V_{G,PP} = V_{GMIN}$ and $V_{D,PP} = V_{DMAX}$, being V_{GMIN}, V_{DMAX} the minimum gate and maximum drain voltages of a particular operative regime. It is interesting to notice how this condition typically coincides with the one reached by the device load line (high-drain and low-gate voltage peaks) at the maximum output power in the application as HPA [2].

In this paper, a similar concept is applied at the amplifier level: a double-pulse measurement procedure is adopted, where the PP is obtained as a combination of supply and RF pulses, leading to large-signal (LS) characterizations of microwave PAs at controlled charge-trapping states. Moreover, since the average power dissipated by the PA can also be also controlled by means of the proposed setup by properly adjusting the parameters of the repetitive excitation patterns, the characterization is also carried out in the same thermal condition of the actual application.

The suggested measurement procedure is applied here for the characterization of an X-band GaN monolithic microwave integrated circuit (MMIC) PA operating in a pulsed-mode envelope tracking (ET) regime for high-efficiency radar applications with radar pulse shaping (i.e., pulse modulation) [15]–[18]. It is worth recalling that the conventional characterization of such amplifiers is still based on static approaches, where the PA is dc biased (static bias supply) at several different supply-voltage levels in the range to be later used in the dynamic supply operation; for each bias level, an RF continuous-wave (CW) power sweep is performed to collect a set of AM–AM, AM–PM PA characteristics (each sample obtained under constant envelope amplitude operation). The multibias characteristics obtained with this conventional technique are not representative of the PA operation under operative dynamic supply modulation with modulated RF signals, since both the thermal and trap states of the PA are highly different than those of the operative ones. The proposed setup overcomes these limitations, since both the supply voltage and the RF signal can be instantaneously modulated, during the AM–AM, AM–PM characterization phase, to reproduce the operating thermal and trap state of the final dynamic regime.

The characterization data measured with the proposed setup are used for the identification of a proper predistortion function for the linearization of the ET amplifier. The obtained results demonstrate that the proposed characterization of the PA with controlled charge-trapping (and thermal) state is clearly more representative of the PA operative condition rather than the conventional measurements.

Preliminary results of this activity were described in [19]. This paper represents an expansion over [19], featuring many additional information.

1) The proposed setup is described in more detail, including the calibration process.
2) Additional measured data are proposed, including the device supply current.
3) Additional discussions about the modulation of the trap state with respect to different operative regimes are provided.
4) PA trap-related performance sensitivity to signal amplitudes and time constants are presented and discussed in more detail, with additional measurement of the PA gain.

This paper is organized as follows. In Section II, the setup is accurately described. Section III describes the proposed PP technique for the characterization of the PA under controlled thermal and trapping states. In Section IV, the dynamic AM–AM and AM–PM characterizations of a GaN PA performed with and without the PP are presented and compared, and some discussion on the trap-state modulation is proposed. Section V is dedicated to the validation of the proposed technique by using the measured data for the identification of a multilevel digital predistortion (DPD) characteristic for the PA linearization, when operating in a modulated pulsed radar regime with ET. Finally, in Section VI, the exploitation of the setup for additional investigations on the trap-related performance degradation of the PA is described and some conclusions are drawn.

II. DESCRIPTION OF THE MEASUREMENT SETUP

As described in the introduction, the proposed measurement setup is developed for the LS characterization of GaN-based PAs under controlled thermal and charge-trapping states. Due to the very high power density of GaN processes, the majority of GaN PAs are usually operated in the pulsed mode (e.g., radar applications) or with high-PAPR signals (e.g., highly spectral efficient telecom signals): in this way, the system thermal design is eased, due to the relatively small average

dissipated power, whereas the PA delivers a very high-peak RF power, as required by the applications. Thus, a setup for the characterization of such amplifiers has a great benefit from the availability of a pulsed supply and an RF source capable to synthesize fast-modulated signals. Moreover, the accurate synchronization between the syntheses of the supply and of the RF signals at the PA ports is needed. Finally, the availability of both amplitude and phase information of the LS operation of the amplifier is highly desirable, with respect to a standard scalar LS characterization.

The proposed setup meets these requirements by adopting the structure described in Fig. 1. For its implementation, we used the vector signal transceiver (National Instruments PXIe-5644R VST), which is an instrument that includes a vector signal generator (VSG) and a vector signal analyzer (VSA). The VSG is capable to synthesize arbitrary modulated RF signals with 80-MHz instantaneous analog bandwidth. The modulated signal is generated at baseband in the digital domain, processed by a 16-b 120-ms/s DACs, and up-converted to RF by an internal I/Q single-stage up-converter followed by a 100-dB attenuation/gain control block. At the receiving section, the VSA operates a down-conversion with a zero-IF I/Q down-converter, followed by the digitalization by means of 16-b 120-ms/s ADCs and the complex channel equalization and signal analyses performed by the internal field-programmable gate array (FPGA). The two local oscillators (synthesizers) of the internal up/down-converters can be locked to the same reference clock, sharing in this way the same start triggers and phase coherency, which is necessary for an accurate characterization of the DUT in amplitude and phase.

The VST output frequency ranges between 65 MHz and 6 GHz: for the X-band PA test, additional up- and down-conversion stages have been implemented externally with commercial off-the-shelf components. As described in Fig. 1, the up-converter is composed of a doubly balanced diode mixer (Minicircuits ZX05-153MH-S+), an image rejection filter and a driver amplifier (Agilent 83020A). The down-converter is composed of a 50-dB coaxial attenuator, a doubly balanced diode mixer (Minicircuits ZX05-153MH-S+ as the up-converter), and a low-pass filter. The 50-dB attenuator is needed for the characterization of PAs with output power up to 46 dBm. The two converters share the same local oscillator (LO) (13-dBm LO power) for the required phase coherency. Moreover, the external LO is also locked to the same 10-MHz reference clock of the VST frequency synthesizers. The overall setup implements dual-step-up- and down-conversions with the same phase reference for all the LOs: the signal is generated at 1 GHz at section S_A at the VST output and analyzed at 1 GHz at section S_B at the VST (VSA) input. The external LO frequency is set to 10.7 GHz. Due to the phase locking of the frequency sources, the DUT can be characterized at X-band (9.7 GHz = 10.7 GHz − 1 GHz = LO − IF) with the VST working at 1 GHz (IF) by means of a simple calibration process.

The mixers and the driver amplifiers in the external up- and down-conversion sections were selected for linear operation up to the maximum input driving power delivered at section S_1 at the DUT input and the corresponding power level at the DUT output (S_2). The IMR and LPF filters provide additional rejection of unwanted mixer products.

A. Calibration

The first calibration step is an automatic calibration of the VST as described in the instrument manual [20]: this calibrates the setup in amplitude and phase at sections S_A and S_B. The selected operative frequency of the VST is 1 GHz.

Then, the X-band measuring system reference planes must be shifted to S_1 and S_2, by means of a calibration procedure aimed at de-embedding the up- and down-converter sections. This calibration is eased by the mentioned selection of mixers/driver for the linear operation within the DUT measurement range since the system is used for a narrowband measurement around the selected X-band carrier frequency. Thus, an assumption of constant group delay of the up/down-converting sections can be adopted for the calibration procedure and then verified.

The external up-converter section is connected at section S_A, the VSG output power at 1 GHz is swept from small signal to LS, and its output is measured with a spectrum analyzer (previously calibrated with a power meter) connected at section S_1: the measured nominal transducer gain $G_{UP} = 23$ dB of the external up-converter (1–9.7 GHz) is almost constant (less than 0.1 dB of gain compression) up to 20 dBm of power at the DUT input section S_1. Moreover, all the spurious mixer products at section S_1 are more than 40 dB under the useful signal at 9.7 GHz and will not excite any significant nonlinearity of the DUT. This procedure was performed on a 40-MHz bandwidth around 9.7 GHz, showing an almost flat frequency response as expected. The collected data are used for the amplitude calibration of the setup at port S_1, which is the new amplitude-calibrated input reference plane of the measuring system. The following step is the characterization of the external down-conversion section from S_2 to S_B. The 50-dB attenuation section is measured at X-band with a VNA, while the remaining mixer and low-pass filter section is characterized (at variable amplitude and frequency) with an additional RF source at the X-band and with the spectrum analyzer. (The external up- and down-converters have very similar performance since it exploits identical mixers.) The overall down-converter exhibits a nominal gain $G_{DW} = -61$ dB (50 dB from the attenuator) with a linear behavior (less than 0.1 dB of gain compression) up to 46 dBm of input power at section S_2. This response is almost flat in a 40-MHz bandwidth around 9.7 GHz.

In Fig. 2, the measured normalized gain and phase of the setup are shown as a function of frequency (@20-dBm input power for the trace in Fig. 2) and the input power (@9.7 GHz for the trace in Fig. 2). The data provided in Fig. 2 represent the response on the setup between sections S_A and S_B (up/down-converting sections) and is practically obtained inserting a zero length thru as DUT.

As a consequence of the design choices and the relatively small bandwidth, the amplitude plots show limited variations in both amplitude and frequency domains. The practically flat
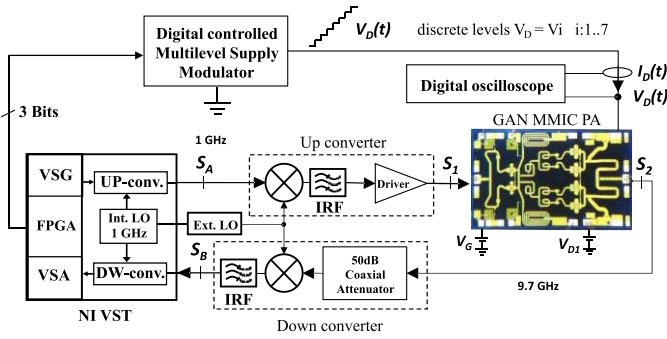
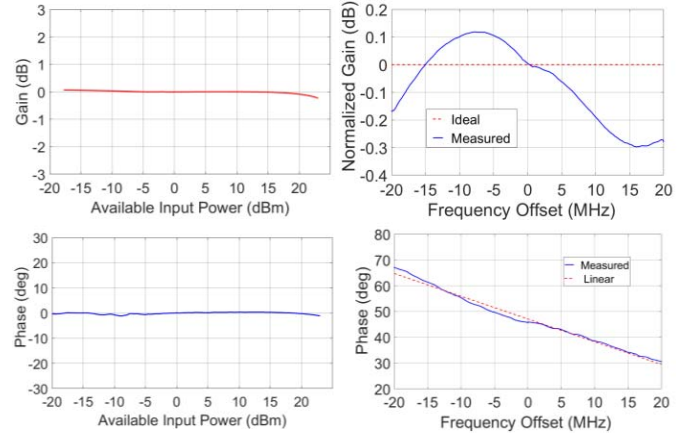Fig. 1. Schematic description of the setup with the MMIC DUT.

Fig. 2. Normalized amplitude and phase response of the setup between sections S_A and S_B (i.e., response of the setup before de-embedding of the X-band up/down-converting sections).

Fig. 3. Verification of the system with a 40-MHz signal transmitted around the 9.7-GHz carrier.

system phase response over the amplitude swing proves linear operation (very little AM–PM conversion) of the external up- and down-converter sections as designed. The constant group delay over the small measurement bandwidth is also verified by the linear variation of the phase versus frequency: practically, the setup does not introduce the phase distortion over the measurement bandwidth and within the dynamic range required for the characterization of the PA DUT. The measured data of the up/down-converter sections response (function of amplitude and frequency) shown in Fig. 2 are stored in the software (LabVIEW VI) developed for the set-up control and automatically de-embedded from the measurement. In this way, the also observed small gain and phase variations over amplitude and frequency shown in Fig. 2 are de-embedded from the measurements.

A verification of the calibration is proposed in Fig. 3. A zero-length thru is made between sections S_1 and S_2, and a 40-MHz signal (frequency-chirped sinusoid) is synthesized by the VSG and measured (at X-band) by the setup. The power of the signal at the DUT input section S_1 is 20 dBm. As shown in Fig. 3, the measured signal spectrum is undistorted within a 40-MHz bandwidth around the central frequency of 9.7 GHz. The measured error between input–output measured signals of Fig. 3, computed in terms of normalized root-mean-square error is 2.82%.

It is worth noticing that the knowledge of the absolute phases in sections S_1 and S_2 is not necessary, since the PA to be measured can be considered a time-invariant component; thus, no additional calibration steps are needed.

B. Supply Path Control and Synchronization

The instrument also features a programmable internal FPGA with 24 digital I/O channels that share the same reference clock used by the VSG and VSA. In the proposed setup, the internal FPGA is used to generate the digital signals (3 b) that control the multilevel supply modulator (Fig. 1) used to deliver the supply voltage and current to the PA under test. The FPGA control of both supply and RF paths enables the accurate synchronization of the DUT dynamic bias and RF driving signals.

The dynamically variable voltage supply $V_D(t)$ is provided to the DUT by a multilevel supply modulator developed in house as described in [21]. This circuit is directly controlled by
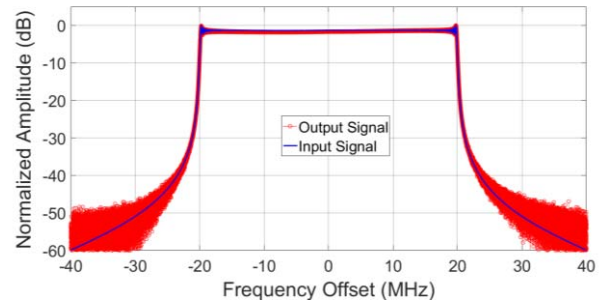
digital signals from the VST instrument FPGA and implements a 3-b power DAC [21]: with three input reference voltage sources $V_{dc,k}$ ($k = 1, \ldots, 3$), the supply modulator can synthesize eight different supply-voltage levels $V_D = V_{Di}$ ($i = 0, \ldots, 7$) (since $V_0 = 0$ V, the useful levels are seven) distributed over a 0–42 V dynamic range and expressed by the equation $V_D = \sum_{k=1}^{3} b_k V_{dc,k}$ where b_k is the binary controlling command ($b_k = 1, 0$) [21]. By changing the values of the input voltage sources $V_{dc,k}$, any possible supply level V_D of interest for the PA characterization (within the circuit dynamic range) can be implemented. Due to the very fast commutations between levels of the power DAC (about 3 ns), pulses as short as 100 ns can be synthesized.

The DUT supply voltage $V_D(t)$ and current $I_D(t)$ are acquired by a digital oscilloscope equipped with wideband voltage and current sensors (Fig. 1).

The I/Q data of the RF signals at S_1 and S_2 are stored in the VST and used for the computation of AM–AM, AM–PM DUT characteristics, whereas the record of $V_D(t)$ and $I_D(t)$ enables the computation of power consumption and efficiency.

Since the FPGA of the instrument controls the generation of both the digital signals at the input of the power DAC and the IQ RF signal, it is possible to add an arbitrary digital delay to the dc path in order to have the RF and supply signals aligned at the DUT RF and supply ports. The correct amount of
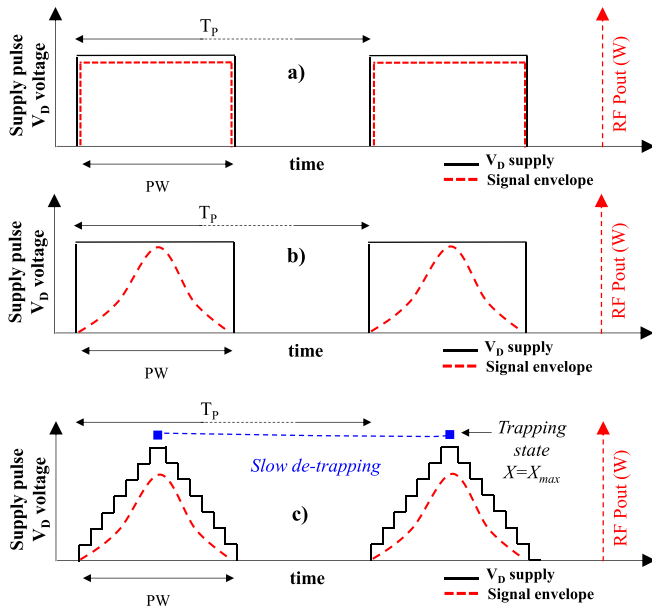
Fig. 4. Different pulsed radar regimes: (a) constant envelope pulses, (b) amplitude-modulated RF pulses with fixed supply amplitude, and (c) amplitude-modulated RF pulses with dynamic-modulated supply. The amount of trapped charges (X) depends on the peaks of supply and RF signal.

delay is found empirically by driving the DUT with nominally synchronized rectangular supply-voltage and Gaussian-shaped RF pulses and by monitoring the PA RF output power (RF acquisition triggered with the RF generation in the VST): the digital delay is then varied until perfect alignment is observed between drain voltage and PA output envelope.

As far as the implementation of the measurement setup is concerned, it is fair to point out that this can be also built with separate VSG and VSA benchtop instruments, properly synchronized with an external FPGA board for the control of the supply modulation and the synchronization with the RF path. Another alternative is represented by the exploitation of board-level digital transmitters/receivers and an FPGA board for supply control, properly connected and synchronized.

III. PREPULSING CHARACTERIZATION OF THE PA UNDER CONTROLLED THERMAL AND TRAP STATES

The PA under test is a 10-W two-stage X-band MMIC designed in the Qorvo 0.15-μm GaN-on-SiC process. A picture of the PA is shown in Fig. 1. This PA was designed by the University of Colorado Boulder in the framework of the DARPA program Microscale Power Conversion. This circuit is unpublished; a quite similar published PA, designed in the same program, is described in [22]. It is a class-AB two-stage PA (3.55 mm $\times$ 2 mm) that delivers more than 10-W output power, with 22 dB of associated gain at $V_G = -2.7$ V and $V_D = 20$ V supply voltage in pulsed operating conditions.

A typical PA operation for radar applications is in pulsed mode with 50-μs pulsewidth (PW) and 10% duty cycle ($T_P = 500$ μs) at 9.7 GHz. Besides typical radar operation with constant envelope RF pulses, advanced radar waveforms with amplitude-modulated radar pulses (i.e., pulse shaping) can be applied to improve spectral confinement [15]–[17]. Fig. 4 describes different pulsed radar regimes: a) constant

envelope pulses, b) amplitude-modulated RF pulses with fixed supply amplitude, and c) amplitude-modulated RF pulses with dynamic-modulated supply.

When amplitude-modulated pulses are used, the envelope tracking of the PA power supply can be used to maintain efficiency [Fig. 4(c)], which would be extremely poor with a constant amplitude supply voltage [Fig. 4(b)], due to the operation of the PA in strong back-off for a large part of the pulse [15]–[18]. Fig. 4(c) shows a discretized multilevel approximation of a Gaussian-like dynamically variable supply profile $V_D(t)$, synchronized with the envelope of the RF pulse. The efficiency is enhanced by forcing the PA to operate at a certain level of gain compression during the entire pulse, which results in nonlinearities that need to be compensated by DPD.

A preliminary AM–AM and AM–PM characterization of the PA at each V_D level is needed to find the DPD coefficients. This characterization should be carried out in thermal and charge-trapping states as close as possible to the ones of the operative regime.

As far as the thermal state is concerned, the proposed setup enables the characterization of the PA in a pulsed regime, under thermal conditions very similar to the actual operating ones. This is due to the capability of the setup to synthesize arbitrary programmable pulsed supply waveforms synchronized with the RF characterization stimulus. Thus, dynamic AM–AM and AM–PM measurements of the PA are performed, by pulsing the supply and simultaneously driving the PA input with an amplitude-modulated RF pulse, which sweeps its entire dynamic range within the supply-voltage pulse duration as described in Fig. 5. This is repeated at different supply voltage levels V_{Di} (Fig. 5).

By properly adjusting T_M (measurement pulse duration) and T_A (measurement pattern period), the same average PA power dissipation as of the actual application can be imposed, thus obtaining a PA characterization in a thermal regime coherent with the radar operation.

However, due to charge-trapping phenomena, this characterization regime (Fig. 5) is not fully representative of the actual operative one. Indeed, since the period T_P (in the range of 10–1000 μs, typical of pulsed radars) is typically shorter than the slow trap-release transient [1]–[5], the GaN PA performance during each level of a given pulse is still affected by the large amount of charge trapping from the previous radar pulse. The proposed interpretation of this mechanism is graphically described in Fig. 4(c) and Fig. 6: the peak of each radar pulse sets the amount of trapped charges (trap state) to a maximum value $X = X_{\text{MAX}}$, corresponding to the high-drain and low-gate voltage peaks reached at the device intrinsic terminals according to the PA dynamic load line at maximum output power.

Thus, we are suggesting that due to the asymmetry of the fast trap capture (occurring in picoseconds) and slow release mechanism (occurring in ms), the trap state rapidly reaches the value $X = X_{\text{MAX}}$ corresponding to the peak voltages of the RF signal, regardless of its very short-time duration: in fact, since the charging rate of the traps is much faster than that of the release rate, a complete filling of the charge-trapping state
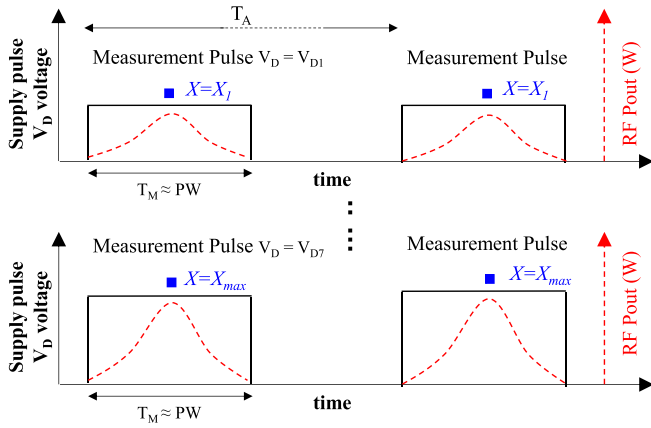
Fig. 5. Pulsed characterization pattern without PP for different voltage levels V_D Different amounts of trapped charges correspond to each level.
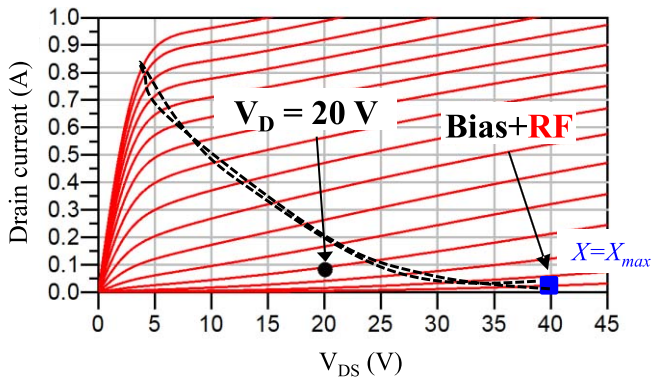

Fig. 7. Pulsed characterization pattern with PP (one for each voltage level V_D).

Fig. 6. Simulated LS load line of the device at maximum V_D and output power superimposed over the dynamic I–V characteristic.

is reached in a few cycles of the RF signal. Since there are several RF cycles for every (even short) supply pulse, the result is a practically instantaneous modulation of the trap state with the peak RF voltage.

In Fig. 6, the simulated operative LS dynamic load line corresponding to the PA peak output power at $V_D = V_{D7}$ is shown with the dashed line superimposed over the dynamic I–V characteristic of a device of the PA final stage. From this instant (peak of the radar pulse), the trap-release mechanism starts, but the trapping state can still be very close to X_{MAX} for the following radar pulse, due to the mentioned slow trap release with respect to typical T_P. It is fair to note that also the pulsed I–V characteristic shown in Fig. 6 (and Figs. 7 and 11) depends on the thermal and trap state. Thus, different I–V plots should be considered for every different LS regimes of the device. The I–V plot used in Fig. 6 (and Figs. 7 and 11) is generated by the design-kit device model and does not necessarily represent the precise device dynamic characteristics in the actual radar operation, since the thermal and trapping states of the pulsed I–V measurement used for the model identification may be different (and are not known). In spite of the approximation involved, the representation in Fig. 6 is useful to intuitively describe the trap-state modulation by the device LS regime, and is used solely to this scope.

It is interesting to observe that the use, during the design phase, of device models capable to reproduce the thermal and
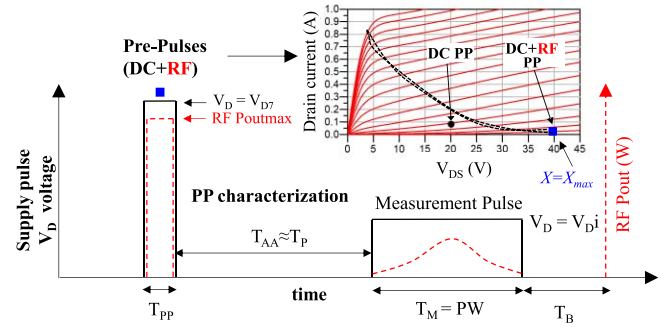
trapping states of a particular operating regime would allow to correctly predict at simulation level the PA behavior observed with the proposed setup: this is surely a very interesting research topic, yet beyond the scope of the activity described in this paper.

The trapping state set by the characterization pattern described in Fig. 5 is not coherent with the one just described for the radar regime, since X is set to X_{MAX} only for the characterization of the highest voltage level $V_D = V_{D7}$. Since the characterization of all other voltage levels is performed with a lower amount of trapped charges than that of the one imposed to the PA by the operative regime, the corresponding measured performance is expected to overestimate the gain and output power that the PA can deliver in the operative regime.

Thus, in order to obtain a more representative characterization of the PA at the different V_D levels under pulsed radar operation, a PP is applied to the PA before the actual "measurement pulse," as described in Fig. 7 to force the trap state to be coherent with the radar regime.

The PP is composed of a supply pulse (dc PP) at the maximum level $V_D = V_{D7}$ provided by the supply modulator and an RF pulse (RF PP) synthesized by the VST that drives the PA to operate at its peak output power.

In this way, the trapping state is set to $X = X_{max}$ at the end of the PP (blue squares in Fig. 7). The actual measurement pulse follows the PP after $T_{AA} = T_P - PW/2$. With this measuring pattern, the characterization of the PA at each V_D is performed with a starting trap state (set by dc + RF PP) that is equal to the one in the radar operating regime ($X = X_{max}$). In the inset of Fig. 7, it is interesting to observe how the combination of the dc and RF PP drives the devices in the PA to operate at the same LS conditions of the radar regime (Fig. 6), thus setting the trapping state to $X = X_{max}$ coherently with the application.

Possible more complex dependences of the charge-trapping state on the applied voltages when below-gate-threshold operation is involved [9] are also implicitly taken into account since the excitation pattern adopted is very similar to the actual radar operation.

It is interesting to point out that this test and characterization technique, which actually proves the instantaneous modulation of the trap state with the peak of the RF signal, represents an extension at the amplifier level of the double-pulse technique

TABLE I
MEASUREMENT CONDITIONS WITHOUT PP

Supply voltage	T_M (µs)	T_A (µs)
$V_{D1} = 3.2$ V	50	125
$V_{D2} = 5.6$ V	50	125
$V_{D3} = 8.8$ V	50	227
$V_{D4} = 11.2$ V	50	333
$V_{D5} = 14.4$ V	50	500
$V_{D6} = 16.8$ V	50	588
$V_{D7} = 20.0$ V	50	806

TABLE II
MEASUREMENT CONDITIONS WITH PP

Supply voltage	T_M (µs)	T_{AA} (µs)	T_{PP} (µs)	T_B (µs)
$V_{D1} = 3.2$ V	50	475	38	437
$V_{D2} = 5.6$ V	50	475	37	436
$V_{D3} = 8.8$ V	50	475	33	442
$V_{D4} = 11.2$ V	50	475	29	446
$V_{D5} = 14.4$ V	50	475	21	454
$V_{D6} = 16.8$ V	50	475	17	458
$V_{D7} = 20.0$ V	50	475	10	465

adopted at the device level by means of the double-pulse I–V technique [2]. While for pulsed-I–V systems, the peak voltages are applied to the DUT with supply pulses, which cannot be shorter than a few tens of nanoseconds due to technical reasons, in the actual set-up peak voltages are applied to the DUT as more flexible combinations of RF LSs (RF input power of the PA synthesized by the VST) on the top of supply pulses (PA supply modulation by the power DAC).

The average power dissipation of the PA during the characterization can be regulated by suitably adjusting the duration of the PP T_{PP}, of the measurement pulse T_M and of T_B, which is the residual time of the PP characterization pattern before the restart of the periodical sequence (see Fig. 7). This is accomplished with an iterative procedure of T_{PP}, T_M, and T_B adjustment, while monitoring the average dissipated power, which can be computed, since the PA input–output and supply powers are instantaneously recorded by the setup, as described in Section II.

With the described measurement pattern, the AM–AM, AM–PM characterization of the PA can be performed at different voltage levels under controlled thermal and charge-trapping states. This is possible due to the capability of the setup to generate arbitrary characterization patterns at the PA RF and supply ports, which are accurately synchronized, due to the unified control of both paths by the FPGA of the instrument directly in the digital domain. For this purpose, the capability of the power DAC [21] to generate arbitrary programmable power pulses is fundamental.

IV. CHARACTERIZATION OF THE PA

The PA characterization at seven different voltage levels of the supply voltage of the second stage V_D ($V_{D1} = 3.2$ V, $V_{D2} = 5.6$ V, $V_{D3} = 8.8$ V, $V_{D4} = 11.2$ V, $V_{D5} = 14.4$ V, $V_{D6} = 16.8$ V, $V_{D7} = 20$ V) is performed at 9.7 GHz with and without the PP. These voltage levels represent the combination

of the three input voltage sources $V_{dc,1} = 3.2$ V, $V_{dc,2} = 5.6$ V, and $V_{dc,3} = 11.2$ V.

The characterization plots of the PA for each voltage level were measured with the technique described in Section III (by pulsing the supply and simultaneously driving the PA input with an amplitude-modulated RF pulse in a periodic regime, as described in Figs. 5–7): the characterization was performed with increasing supply-voltage levels and a 30-s interval was inserted between the measurement of each level. It has been verified that the variation of the duration of this interval does not have any influence on the measurements, as far as the same thermal dissipation of the DUT is imposed with the described iterative procedure (T_{PP}, T_M, T_A, T_{AA}, T_B adjustment), and the base plate temperature is kept constant. The combination of time constants adopted to maintain a constant average dissipated power ($P_{DISS} = 300$ mW) in each measurement is listed in Tables I and II, for the characterization without ad with the PP, respectively.

The AM–AM and AM–PM plots obtained with the described shaped AM RF pulse excitations can potentially show some hysteresis, if both the rising and falling edges of the RF AM pulse are plotted in the same graph, due to possible asymmetries of the PA behavior along the first and second parts of the RF pulse. For the sake of simplicity, the curves of Figs. 8–11 are plotted by considering the upside part of the AM RF pulse only, while a dedicated discussion on possible asymmetries during the measurement pulse is presented in Section IV-A.

In Figs. 8 and 9, the measured gain characteristic of the PA in amplitude (AM–AM) and phase (AM–PM) is shown.

Fig. 10 shows the PA output power versus the input available power. In Figs. 8–11, there is one plot for every voltage level, with the solid lines referring to the measurement with PP and the dashed lines to conventional measurement without the PP.

It is important to notice that for these measurements, T_M, T_A, and T_{PP} were selected in order to have the same PA power dissipation of the reference radar regime: thus, the thermal states of the two sets of measurements described in this section are coherent and the observed differences can be reasonably explained by the different trapping states (PP condition versus no PP).

Remarkable differences between the two sets of data are observed, especially at low-power levels and low V_D, indicating a strong influence of the peak-trapping state on the PA performance under variable supply conditions. The highest performance variations due to the trapping mechanism activated by the PP are observed at the lowest supply voltages (V_D), since for these voltage levels, the variation in the trap state X with respect to X_{max} set by the PP is maximized (The trap state is somehow proportional to the voltage peak.) For instance, by considering the small-signal condition, the peak drain voltage setting the trap state X is the supply voltage itself in the case of no PP, whereas during PP measurement, it is about 40 V, which sets the trap state to X_{max}. At the highest voltage levels, these differences tend to become progressively less significant.

As an example, 12 dB of gain difference and 37° of phase difference are observed between the characterization
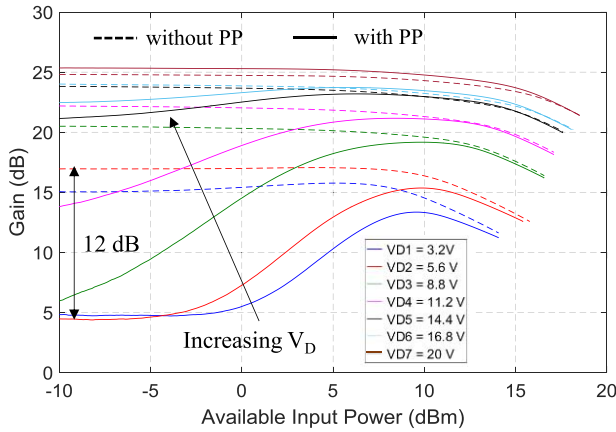
Fig. 8. Available gain of the PA at different V_D: comparison between measurement with (solid lines) and without (dashed lines) PP.
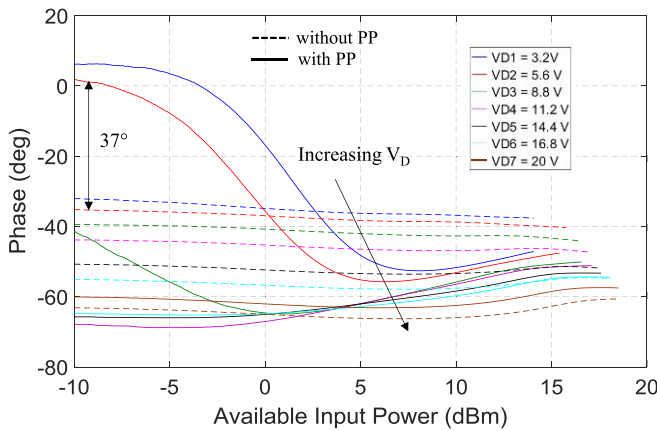

Fig. 9. Phase of the PA gain at different V_D: comparison between measurement with (solid lines) and without (dashed lines) PP.
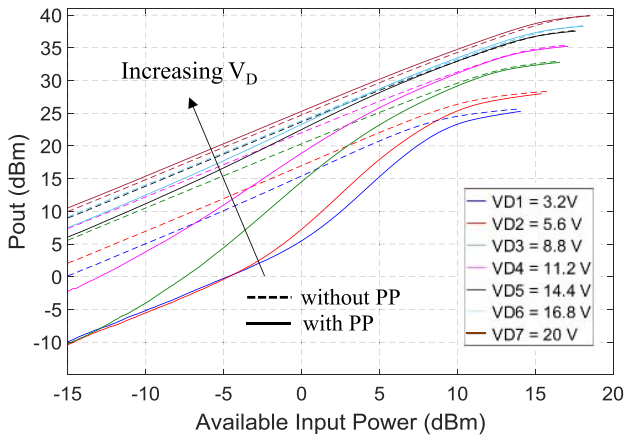

Fig. 10. PA output power at different V_D: comparison between measurement with (solid lines) and without (dashed lines) PP.
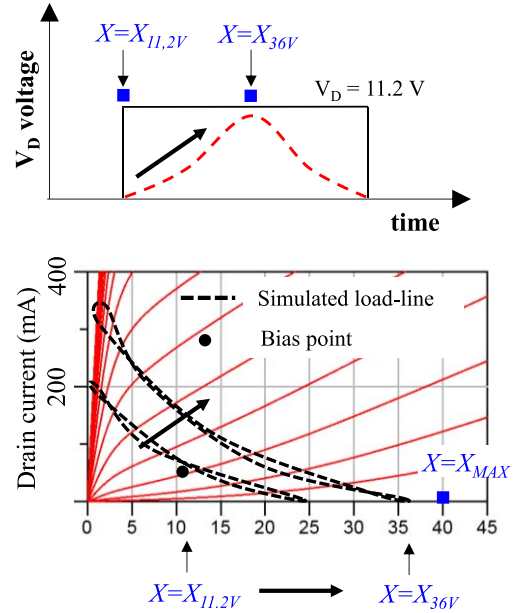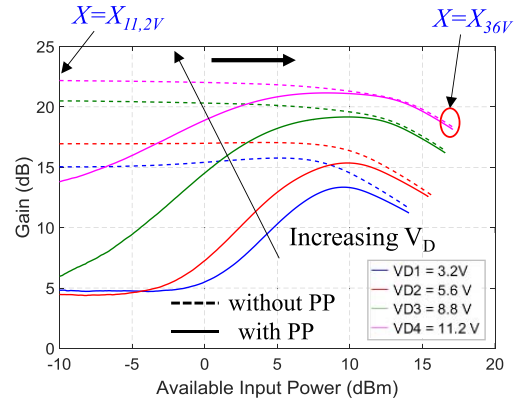

Fig. 11. (Top) Measured gain for the first four V_D levels with (solid lines) and without (dashed lines) PP. (Bottom) Modulation of the trapping state during the measurement pulse for the measurement without the PP.

with and without the PP for the voltage level $V_{D2} = 5.6$ V. As expected, the characterization without the PP overestimates the PA gain and output power performance with respect to the measurement with the PP that forces a larger amount of trapped charge in the PA active devices.

Additional insights on the trap-related PA performance can be gathered from these comparisons: in the top of Fig. 11, the characterization of the gain for the first four voltage levels only is proposed for the sake of simplicity.

It is interesting to observe that the differences between PP and no-PP data are very large at small input power, but tend to zero at high-gain compression. This behavior can be explained as follows. In the PP measurement (solid lines), the trap state starts from a level $X \approx X_{\max}$ (slow release) from the beginning of the measurement pulse, then at low-input power. On the other hand, in the measurement without PP, the trapping state starts from a value corresponding to the supply-voltage level and is instantaneously modulated by the dynamic load line during the measurement pulse.

As an example, looking at the lower graphs of Fig. 11, for the measurement at $V_D = 11.2$ V, the trapping state starts from a value $X = X_{11.2 \text{ V}}$ corresponding to 11.2-V supply at small signal and is modulated by the load line reaching increasing peak voltages along the measurement pulse. As can be seen in the lowest graph of Fig. 11, at the peak of

the characterization pulse, the simulated intrinsic load line reaches a maximum voltage level of 36 V, which is fairly close to the PP peak voltage (about 40 V). Consequently, the corresponding trapping state $X_{36 \text{ V}}$ is much closer to the one set by the PP $X = X_{\max} = X_{40 \text{ V}}$, and for this reason, the gain at high compression is very similar, as shown in the measurement of Figs. 8 and 11.

Observing Figs. 8 and 10, it is fair to notice that for the last voltage level $V_{D7} = 20$ V, the output power and then the gain measured with the PP are slightly higher than without the PP (difference of about 0.3 dB). According to the proposed theory of instantaneous modulation of the trapping state with the peak drain voltage, for the highest supply voltage level V_{D7}, the gain/P_{out} measured with and without the PP should be equivalent, since in both cases X is set to $X_{\max}$ before the measurement pulse. (In the case without PP, X is set to $X_{\max}$ by the previous measurement pulse.) The difference shown by actual measurements can be due to the combination of different causes, as: small differences in the actual peak voltages reached in the two different regimes, small discrepancy of the thermal state of the two regimes and generic setup accuracy limitations.

Another parameter that is measured by the setup is the instantaneous supply current of the PA, which is an important indicator of the trapping state of devices in the PA [13]. The measured PA drain current (with and without PP) correspond-ing to the gain characterization shown in Figs. 8 and 11 is observable in Fig. 12.

The observed current reduction due to the PP is significant at small input power levels, whereas for the instantaneous trap modulation mechanisms discussed above, it tends to decrease with higher input power, resulting in similar gain and P_{out} characteristics at high compression (see Fig. 8, 10, and 11). This trap-assisted reduction of the current is caused by drain-lag effect that has been largely observed in GaN HEMT: the novelty in this experiment is that the trap charge is controlled by the peak RF voltage under the LS operation of the device, rather than the bias voltage. In Table III, the measured drain currents at the beginning of the measurement pulse (i.e., at small signal levels, i.e., -10 dBm of available input power) are listed for the first four voltage levels along with the corresponding PA gain. (The data in Table III come from the same characterization of the gain shown in Figs. 8 and 11). The very strong current collapse correlates with the large differences in small-signal gains.

By observing the measured gain and current characteris-tics shown in Figs. 11 and 12, it is interesting to notice that the effect of the charge trapping induced by the PP is practically a transformation of the PA operation from the designed class-AB to class-C due to the induced self-pinching of the device. As a consequence, the nonlinearity of the gain characteristics is more pronounced and more difficult to linearize. Moreover, since the gain/current degradation phenomena could be interpreted as a trap-induced pinch-off shift of the HEMT, the dynamic control of the gate supply can be considered as an interesting mechanism to be exploited in order to improve the DPD for the linearization of the PA.
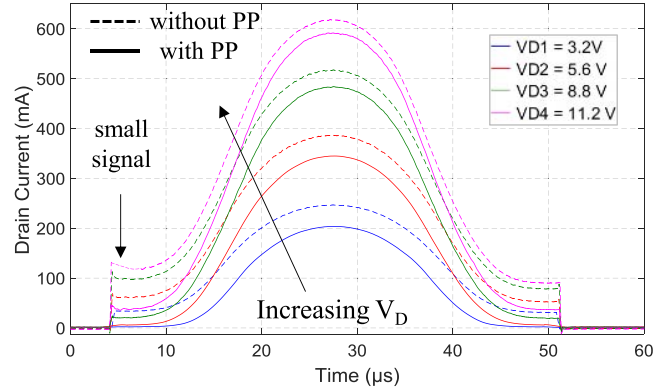

Fig. 12. PA drain current during the measurement pulse for the first four V_D levels.

TABLE III
PA DRAIN CURRENT AND GAIN AT "SMALL SIGNAL" ($P_{\text{AV}} = -10$ dBm)

V_D level	Drain current			Gain		
	NO PP	PP	Variation	NO PP	PP	Variation
3.2 V	34 mA	3 mA	-91%	15 dB	4.8 dB	-10.2 dB
5.6 V	61 mA	7 mA	-88%	17 dB	4.5 dB	-12.5 dB
8.8 V	97 mA	20 mA	-79%	20.5 dB	5.5 dB	-15 dB
11.2 V	122 mA	38 mA	-69%	22.2 dB	11.5 dB	-10.7 dB

Comparisons between the two data sets shown in this section again demonstrate the assumption of instantaneous trap state modulation with the peak RF voltage.

It is fair to notice that the described behavior (Class-C like) is very similar to what observed by Pedro *et al.* in [23] with different (CW) setups and confirms their interpretation of trap-related low-frequency dispersion justification of such characteristics of GaN PAs. In addition, with the proposed setup, any thermal-related influence on the observed behavior is completely eliminated, since, as previously pointed out, the thermal states of the two sets of measurement (PP and no PP) are coherent; thus the observed differences are due only to different trapping states.

A. Hysteresis of AM–AM and AM–PM Plots

If the PA thermal or trapping states change during the Gaussian-shaped RF measuring pulse, the AM–AM and AM–PM plots would show some hysteresis if both the rising and falling edges of the RF AM pulse are plotted in the same graph. The same mechanism would show asymmetries in the rising and falling edges of the complete profile of the instantaneous drain current during the pulse (Fig. 12).

The measured data of the PA characterized as described in Sections III and IV have shown weak hysteresis in the gain plots corresponding to the highest voltage levels, and almost negligible hysteresis for lowest levels. This behavior is confirmed by also observing the plots of the drain current shown in Fig. 12, where the bell-shaped current profiles are almost symmetrical for the first three voltage levels, whereas a moderate asymmetry appears for the highest voltage. It is worth observing that since the measurement pattern period is short compared to the trap-release time constants, the trap state
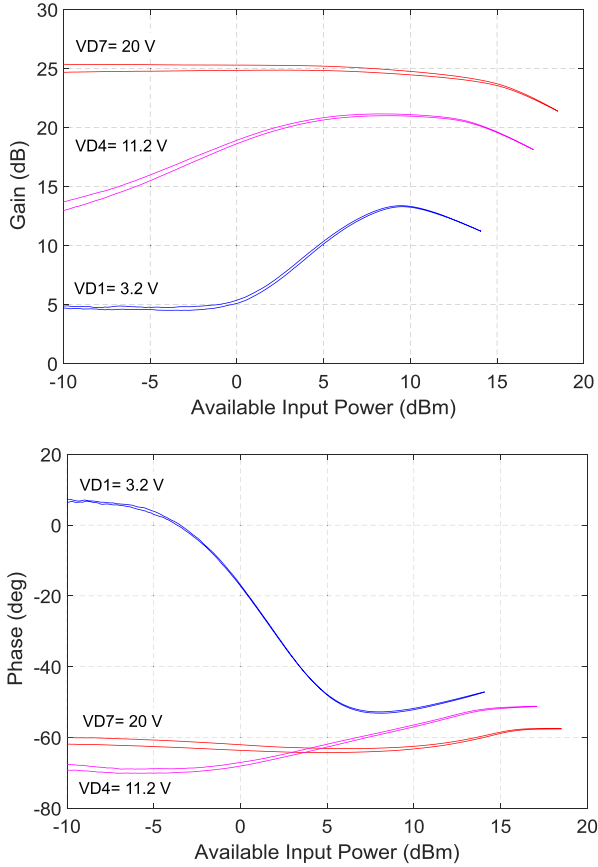
Fig. 13. (Top) Hysteresis of gain and (Bottom) phase plots at three different voltage levels, characterization with the PP.

Fig. 14. Normalized AM–AM and AM–PM characteristics of the multilevel DPD.

is mainly constant and determined by the peak voltage reached in the PP (or in the previous radar pulse). Indeed, very little release of traps happens between successive pulses.

Thus, the observed asymmetries must be due to little temperature variations during the RF AM pulse (actually lasting some tens of μs, i.e., a time scale compatible with the occurring of some thermal dynamic effects). According to this explanation, the hysteresis/asymmetries are more evident for higher voltage levels, corresponding to higher dissipated power and thus higher temperature variations within the pulse.

In Fig. 13, the plots of the gain and phase (characterization with the PP) for three different voltage levels plotted considering both the rising and falling edges of the RF pulse are shown. The maximum hysteresis is limited to a maximum of 0.6 dB (around 25 dB) and 2° (around −60°) for the gain and phase of the highest voltage level, respectively; increasing of the hysteresis with increasing voltage level is also noticeable.

V. VALIDATION RESULTS

As discussed in the previous section, the comparisons of the measured performance of the PA obtained with and without the PP show relevant performance degradation of the PA (i.e., lower gain and output power) when the trap state is preconditioned by the PP to a level ($X = X_{\text{MAX}}$) which is coherent with the PA state in the ET pulse-shaping radar regime of the target application.
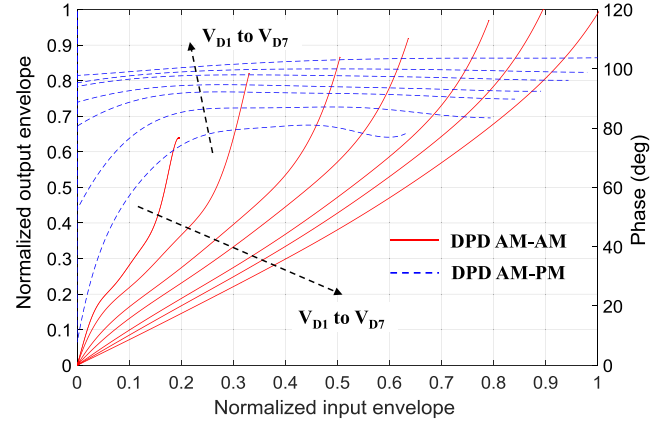
To validate the capability of the proposed PP characterization to be more representative of the PA performance in the target operative condition, both measured sets obtained with and without the PP are used for the identification of complex DPD coefficients adopted for the linearization of the PA operating in the pulse-shaping ET regimes described in Fig. 4(c). This is done by simply inverting the measured AM–AM and AM–PM characteristics for each discrete voltage level and using them to identify the approximating complex polynomials by means of least-squares curve fitting. To this aim, the characteristics plotted exploiting only the rising edge of the characterization AM RF pulse were used; thus the limited hysteresis observed in Fig. 13 was not considered.

The adopted memoryless polynomial model is defined by

$$z(n) = \sum_{k=1}^{K_i} a_{k,i} x(n) |x(n)|^{k-1} \tag{1}$$

$$a_{k,i} = |a_{k,i}| e^{j\angle a_{k,i}} = a_{k,i}(V_{D_i}), \quad i = 1, \ldots, 7 \tag{2}$$

$$V_{Di} = \mathcal{F}_D(|x(n)|), \quad i = 1, \ldots, 7 \tag{3}$$

where $x(n)$ and $z(n)$ are the baseband original and predistorted signals, respectively, and $a_{k,i}$ are the complex polynomial coefficients dependent on the instantaneous bias voltage V_{Di}.

The order K_i of the predistorter polynomials is the same $K_i = 9$ for all the voltage levels $i = 1, \ldots, 7$.

The instantaneous voltages V_{Di}s are selected by the input signal amplitude $|x(n)|$, according to a discretized-shaping function $\mathcal{F}_D$ that optimizes the PA efficiency.

In Fig. 14, the predistorter normalized AM–AM and AM–PM characteristics for the seven supply levels described by the polynomials in (1) are shown.

It is interesting to notice that the same setup is used as the actual radar transmitter operating with ET and digital predistortion. Indeed, the predistorter complex polynomial coefficients and the supply shaping function are stored in the FPGA of the VST and used to implement the DPD and ET control, as described in [15] and [21].

In Fig. 15, the ET transmitter gain is shown for the following conditions: 1) without DPD; 2) with the application of the DPD identified from data without the PP;
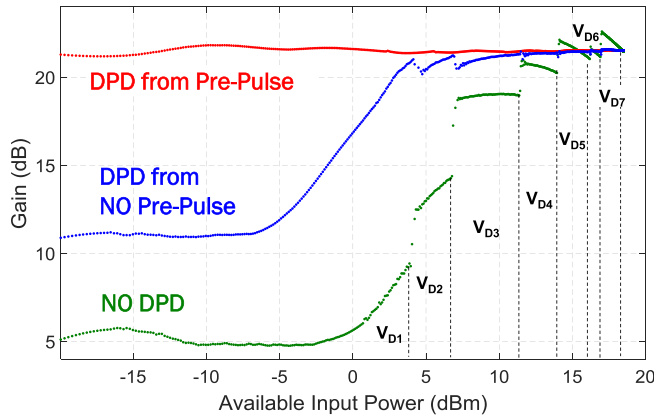
Fig. 15. Linearization of the gain of the ET radar transmitter exploiting characterization data obtained with and without the PP.
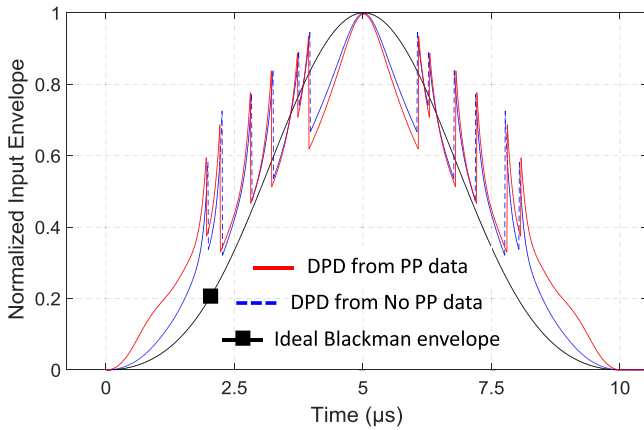

Fig. 17. Transmitter output spectrum: ideal, without DPD, with DPD from PP data, and with DPD from no-PP data.

Fig. 16. Envelope of the input RF pulse: ideal Backman envelope and predistorted versions from data obtained with and without the PP.

and 3) with the application of the DPD identified from PP data.

Fig. 15 shows clearly that the DPD identified from the data acquired without PP fails to linearize the ET PA, especially at low-input power and V_D levels, where the differences due to trapping effects are more prominent (see Fig. 8 and previous discussion).

In particular, the gain compensation provided by the DPD identified from no-PP data (data obtained without the PP) fails to linearize the PA gain at low levels, since the exploited characterization measurements overestimate the PA gain due to the lack of the proper control of the trapping state during the measurement. This can also be appreciated in Fig. 16, where the normalized envelope of the RF input signal is shown in the time domain: the predistorted signal from PP data provides a larger gain expansion with respect to the ideal envelope shape to be transmitted (the Blackman window shape in this case) than the predistorted signal from no-PP data.

Finally, the output spectrum of the transmitter is presented in Fig. 17. The output spectrum obtained with the DPD from PP and no-PP data is compared with the ideal one (Blackman pulse shape) and with the one without DPD. This result
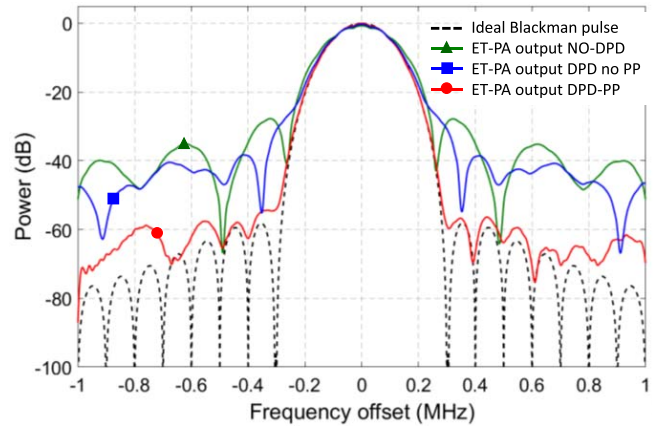
indicates that the characterization with controlled charge-trapping state (i.e., with PP) is clearly more representative of the PA operative conditions, leading to nearly optimal PA linearization.

It is fair to notice that a simple open-loop DPD, without any feedback and coefficient optimization through a learning architecture, was intentionally chosen, since this represents the simplest tool in order to perform a fair comparison between the performances obtained from the two data sets (with and without the PP).

Certainly, the use of a feedback-based DPD coefficient optimization would improve the performance in both cases, but would not be useful for the comparison between characterization data. (See the discussion about the use of this data with PA behavioral models in the last section.)

A. Preliminary Experiment With Telecom Signals

The described PA characterization was carried out with a combination of T_{PP}, T_M, and T_A that reproduced the PA thermal and trap state in a deterministic operative radar regime. The DPD extracted from this characterization was therefore optimized for that particular periodic regime. The application of the proposed technique to the linearization of communication signals would require a specific characterization pattern taking into account the statistics of the telecom signal [PAPR, probability density function (PDF), and complementary cumulative distribution function (CCDF)] in order to reproduce the average thermal and trap-state conditions of the PA. In this context, the best approach is to use the capability of the proposed setup to identify the PA behavioral models to be exploited for the implementation of efficient real-time adaptive DPD strategy as discussed in Section IV. This will likely be the subject of further researches. Nonetheless, by adopting some approximation, a preliminary experiment was carried out with telecom signals. In fact, it can be seen that in the case of the radar signal, the trapping state is periodically adjusted to its maximum level (X_{MAX}) by the peak of the periodic radar pulse. So, in the case of a high-PAPR telecom signal, the signal peaks set the trap state to X_{MAX} with an occurrence that depends on the signal's CCDF and symbol
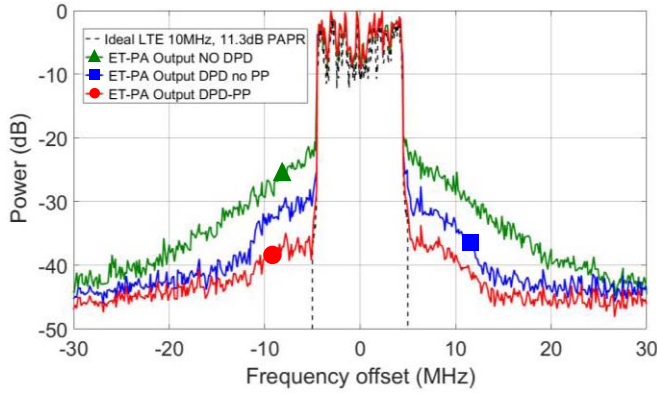
Fig. 18. Transmitter output spectrum for a LTE 10-MHz, 11.3-dB PAPR input signal: ideal, without DPD, with DPD from PP data, and with DPD from no-PP data.

rate. If the average repetition time of this occurrence (which is a statistical quantity) is sufficiently shorter than that of the trap time release (similar to the described radar application), then the characteristics obtained with a PP characterization can give a fair description of the PA also under the ET regime with telecom signals (provided that also the average power consumption of the PA during the characterization is similar to the one under operative condition). In Fig. 18, the comparison of the linearization performance obtained with DPD extracted from PP and no-PP characterization data (both obtained in a thermal regime coherent with the operative one) is proposed, when the PA is operated under ET with a 10-MHz, 11.3-dB PAPR LTE signal.

The PP characterization was carried out with a period T_A (which is roughly the time advance of the PP before the characterization measurement) set to the average value of the peaks' occurrence in a typical sequence of the selected LTE signal, which is about 300 μs. This value is largely smaller than the trap time release, as observed for the radar regime and furtherly discussed with the experiments in Section VI.

Comparisons shown in Fig. 18 demonstrate that the DPD extracted from PP data is more effective for the ET-PA linearization. Thus, even though the proposed characterization regime cannot strictly reproduce the trapping state of the ET-PA with LTE signals, the PP characterization data are still more representative of the actual PA behavior, since they are measured operating the PA in a trapping state more similar to the one of the actual regime.

VI. ADDITIONAL SET-UP CAPABILITIES

The capability of the setup to characterize the PA with arbitrary RF and supply patterns can be exploited for many other additional measurements to investigate the PA behavior related to trap-assisted mechanisms. Some additional experiments performed for a better understanding of the influence of traps on the PA performance are presented in this section. These experiments were performed on a very similar PA (same device periphery and amplifier topology) but from a different foundry run. This PA delivers slightly more peak output power (12 versus 10 W) and shows very similar performance degradation related to trap phenomena.
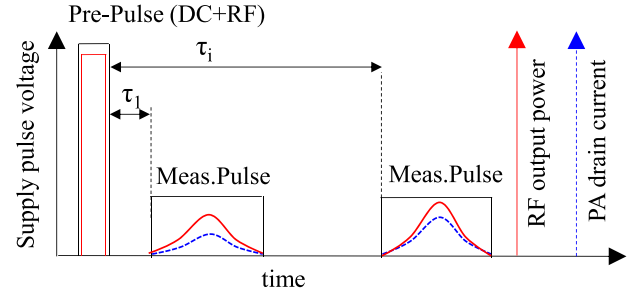

Fig. 19. Characterization measurement pattern with variable PP time advance τ_i for the investigation of the trap-release duration.
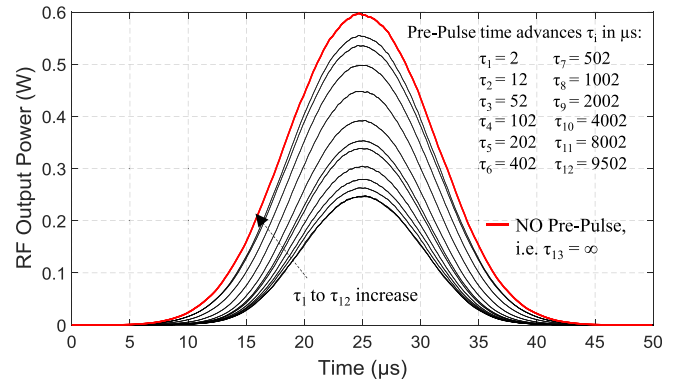

Fig. 20. PA output power for level $V_D = V_{D2} = 5.6$ V at variable PP time advance τ_i for the evaluation of the trap-release mechanism duration.

In the first experiment, described in Fig. 19, the length of the trap-release mechanism is investigated by measuring the PA performance with PPs of fixed supply amplitude and RF power (PP with $V_D = 20$ V, $P_{RF} = 12$ W in this case), while the PP time advance (τ_i) with respect to the measurement pulse is varied.

In Figs. 20–22, the measured PA output power, drain current, and gain (for $V_D = V_{D2} = 5.6$ V) when varying τ_i starting from 2 μs are shown. At increasing time advance, the PA performance improves (larger P_{out}, I_D, and gain), due to the increasing amount of detrapped charges. It can be noticed that the trap-release mechanism is very slow and has not ended after about 9.5 ms.

The thick red curves at the top of the characteristics in Figs. 20–22 represent the PA behavior without the PP applied, hence without any preconditioning of the trap state before the measurement.

It is fair to point out that in this case observed asymmetry in the bell-shaped current waveforms should be mainly due to trap modulation mechanism, rather than device self-heating, since for the selected $V_D = V_{D2} = 5.6$ V, the dissipated power is very low, and does not bring to observable variation of the device thermal state, as observed in the discussion of Fig. 12. Indeed, an accurate observation of the measured drain currents in Fig. 21 reveals an interesting behavior: for measurements up to $\tau_{10} \approx 4$ ms, the current bell-shaped waveforms are perfectly symmetrical, since the trap state of the devices is still dominated by the PP trap capture at $X = X_{max}$ for the
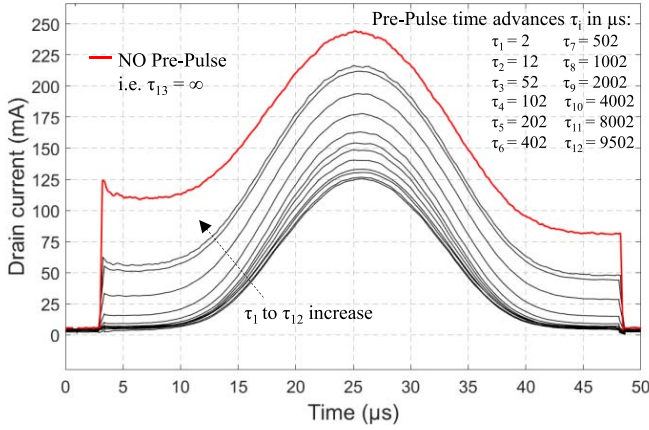
Fig. 21. PA drain current for level $V_D = V_{D2} = 5.6$ V at variable PP time advance τ_i for the evaluation of the trap-release mechanism duration.
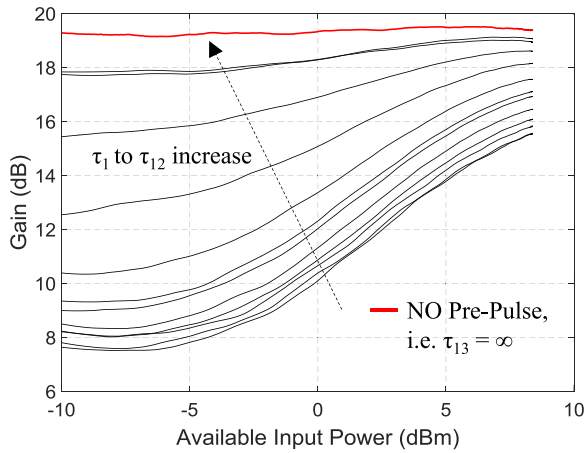

Fig. 22. PA gain for level $V_D = V_{D2} = 5.6$ V at variable PP time advance τ_i for the evaluation of the trap-release mechanism duration.
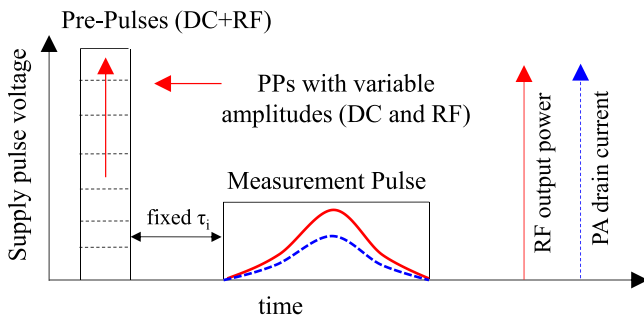

Fig. 23. Characterization measurement pattern with variable PP amplitude (dc and RF) for the evaluation of the trap-state amplitude sensitivity.

whole measurement pulse duration (and the variation of the thermal state is negligible, due to the low dissipated power at $V_D = V_{D2}$). On the contrary, for larger time advances ($\tau_{11} \approx 8$ ms and $\tau_{12} \approx 9.5$ ms), the amount of detrapped charges becomes significant and the small asymmetry of the current waveforms is due to the modulation of the trapping state during the measurement pulse. The slightly lower values of the drain currents at the end tail of the waveforms with
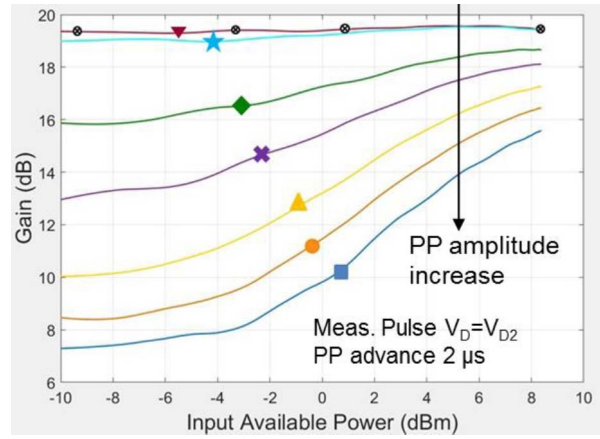

Fig. 24. PA gain for level $V_D = V_{D2} = 5.6$ V at variable PP amplitudes for the evaluation of the trap-state amplitude sensitivity.

respect to the corresponding ones at the beginning indicate that the maximum level of charge capture is not set by the PP anymore, but has occurred at the midpoint of the measurement pulse, where the drain voltage reached its maximum (during the measurement pulse) for the combination of the supply voltage and the RF LS load line. This behavior is more evident in the current waveform measured without the PP (thick highest curve), where the mentioned asymmetry is remarkable. An additional comment is required for this last waveform about the observable slow decrease of the current at the beginning of the Gaussian pulse, which must be surely ascribable to device self-heating. (Trapping mechanism is much faster.) Indeed, differently from all the other measurements in the graph, which were taken in a periodic regime, this measurement (no-PP) was performed with a single-shot pulse (i.e., infinitive PP time advance) and thus, at the beginning of the pulse, the device is colder and consequently its thermal state undergoes a higher variation (that is, observable in the drain current) even in the presence of a small dissipated power ($V_D = V_{D2}$).

The asymmetries discussed in the drain current of Fig. 21 for $\tau_i > 4$ ms are not observed in the corresponding gain curves of Fig. 22, since, as discussed in Section IV, those curves are plotted considering the upside part of the AM RF pulse only.

The same characterization of the trap-release mechanism duration can be performed for different V_D levels and with different PP amplitudes (dc and RF), thus extracting additional information about possible time constants' dependence on signal amplitudes.

In the second experiment described in Fig. 23, the sensitivity of the PA gain, RF output power, and drain current to different PP amplitudes is investigated by measuring the PA performance at a given V_D level, while applying PPs of increasing supply-voltage amplitudes ($V_D = V_{Di}$) and RF power with a fixed PP time advance ($\tau_i = 2$ μs and measurement pulse $V_D = V_{D2} = 5.6$ V in this case).

In Figs. 24–26, the PA gain, output power, and drain current measured for different PP amplitudes are shown. In Figs. 25 and 26, the PP amplitudes are also displayed along with their measured values (dc and RF).
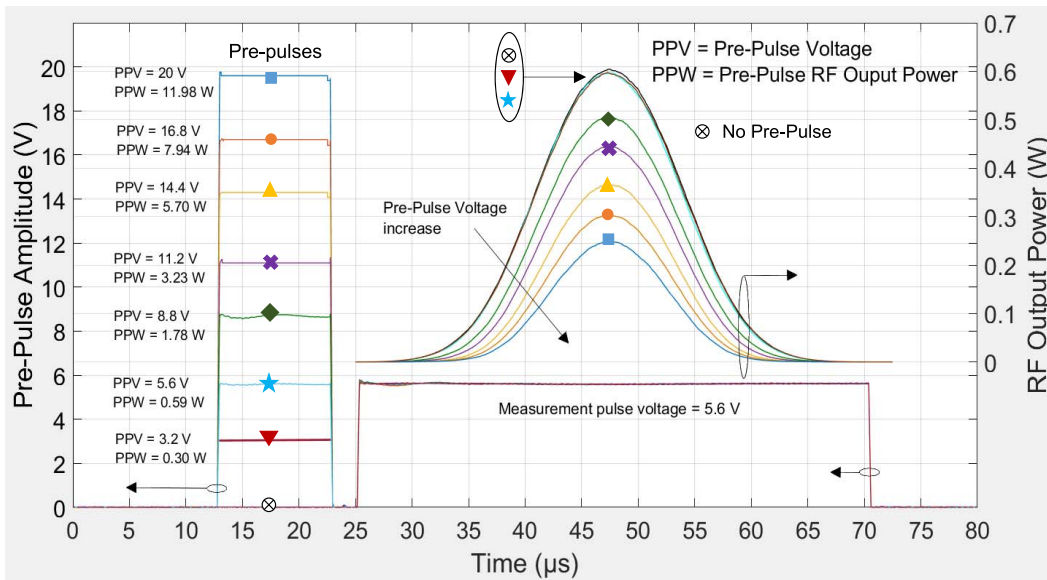
Fig. 25. PA output power for level $V_D = V_{D2} = 5.6$ V at variable PP amplitudes for the evaluation of the trap-state amplitude sensitivity.
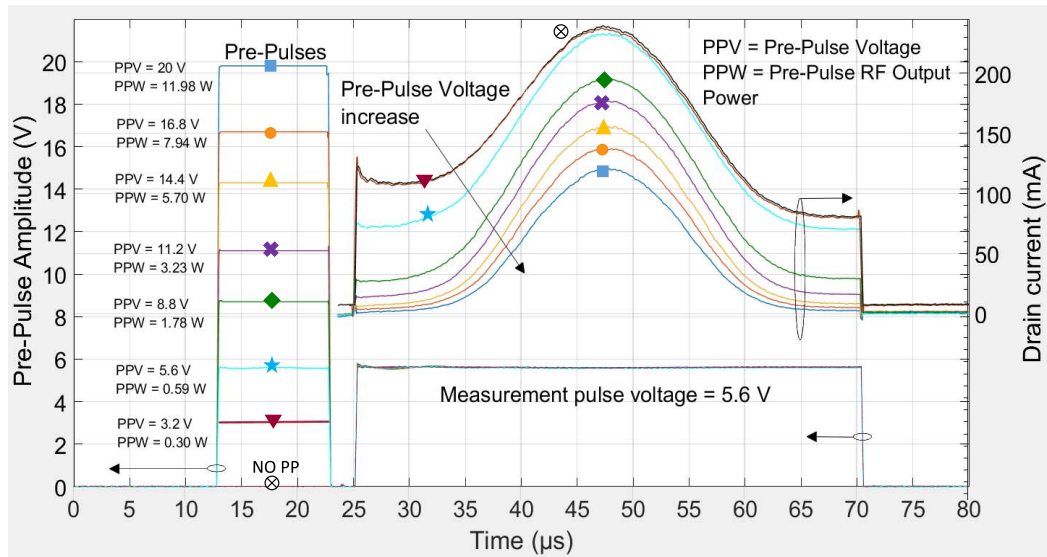

Fig. 26. PA drain current for level $V_D = V_{D2} = 5.6$ V at variable PP amplitudes for the evaluation of the trap-state amplitude sensitivity.

As expected, for amplitudes below the actual measurement pulse with $V_D = 5.6$ V, there is no sensitivity of the PA performance to PP, since the maximum trapping state is set by the measurement pulse itself. On the contrary, for supply and RF PP levels exceeding the measurement pulse, higher amounts of trapped charges preconditioned by the PP induce large gain, current, and P_{out} drops in the measurement pulse.

Finally, the PA performance variation measured in the two proposed experiments are summarized in terms of peak RF output power and peak drain current (peak values of the Gaussian pulse) in Figs. 27 and 28 for the amplitude and time-advance sensitivity test, respectively.

Other similar experiments are possible due to the high flexibility of the proposed setup that enables the characterization

of the PA under arbitrary programmable excitation patterns of synchronized RF and supply stimuli.

This flexibility enables performing the characterization of the PA under controlled thermal and trapped-charge states that can be forced to be coherent with a particular application.

Thus, this setup can be exploited for further insight into the performance degradation of trap-affected PA with respect to signal characteristics. For pulsed radar application, the PA performance variation due to trapping effects when varying radar parameters as the pulse repetition frequency, the duty cycle, the radar pulse shape, and the radar pattern peak-to-average ratio (PAR) can directly be evaluated. For applications in the field of communications, the effects of traps on the amplifier performance when varying the signal PAR, PDF, and CCDF can be assessed: indeed, all these parameters have
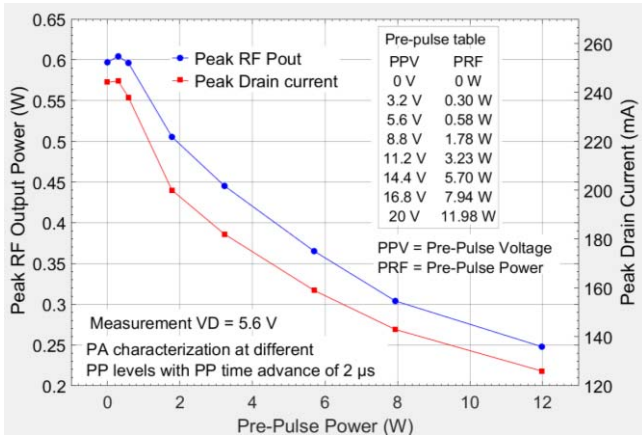
Fig. 27. PA performance sensitivity to PP amplitude: peak output power and peak drain current.
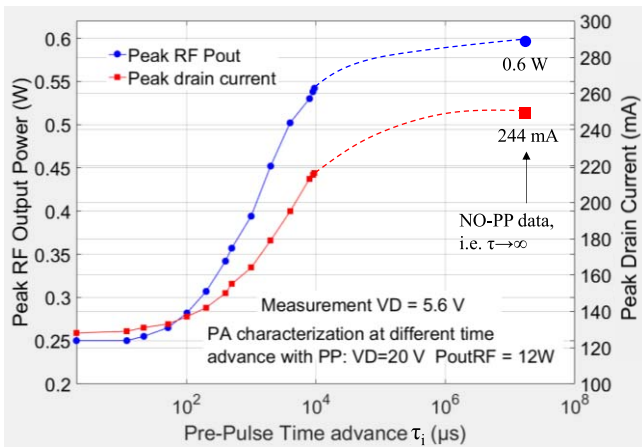

Fig. 28. PA performance sensitivity to PP time advance (τ_i): peak output power and peak drain current.

relevant effects on the PA performance that depends on the sensitivity of the trap state to the signal amplitude and on the values of the time constants of the trap-release mechanisms.

VII. CONCLUSION

The PP technique and setup proposed in this paper, by controlling both trapping and thermal states, have demonstrated to be effective for a PA characterization that gives a better estimation of the circuit performance in the actual application regime. The proposed experiments actually prove the instantaneous modulation of the trap state with the peak of the RF signal in GaN-on-SiC HEMT devices.

The effectiveness of the proposed setup was demonstrated by using the characterization data for the direct identification of the complex DPD coefficients used for ET transmitter linearization in a radar transmitter with pulse shaping.

The same experiments were performed also on C-band GaN PAs described in [24] and [25], exploiting different gate-length processes (0.25-μm GaN-on-SiC pHEMT) of different foundries (United Monolithic Semiconductor). The observed very similar results of these tests confirm the presence of the same effects with another well-assessed commercial-level GaN process, emphasizing the importance of their assessment and characterization, especially when supply-modulated regimes are involved.

Besides this direct use of the characterization data or the direct evaluation of the PA performance under a particular trap and thermal state regime just discussed, the proposed setup can also be exploited to gather measured data as the ones in the experiments described in Figs. 19 and 23 that can be very useful for the identification and validation of PA behavioral models that take into account nonlinear trapping effects, as the one in [26]. These models are useful for the linearization of PAs operating in ET regimes with high-PAPR and wide-bandwidth telecommunication signals. In those operating conditions, only the statistical properties of the PA working regime are known, and an efficient real-time adaptive DPD strategy should exploit accurate HPA behavioral models, since a direct closed-loop approach is unpractical and inefficient with wideband signals. The information of Figs. 27 and 28 regarding the trap state sensitivity to signal amplitudes and the nonlinear duration of the trap-release mechanisms can be exploited for the formulation and identification of behavioral models that would improve the accuracy of DPD for GaN-based PAs (see [27]).

REFERENCES

[1] O. Jardel et al., "An electrothermal model for AlGaN/GaN power HEMTs including trapping effects to improve large-signal simulation results on high VSWR," IEEE Trans. Microw. Theory Techn., vol. 55, no. 12, pp. 2660–2669, Dec. 2007.

[2] A. Santarelli et al., "A double-pulse technique for the dynamic I/V characterization of GaN FETs," IEEE Microw. Wireless Compon. Lett., vol. 24, no. 2, pp. 132–134, Feb. 2014.

[3] J. Joh and J. A. del Alamo, "A current-transient methodology for trap analysis for GaN high electron mobility transistors," IEEE Trans. Electron Devices, vol. 58, no. 1, pp. 132–140, Jan. 2011.

[4] A. Santarelli, R. Cignani, D. Niessen, P. A. Traverso, and F. Filicori, "New pulsed measurement setup for GaN and GaAs FETs characterization," Int. J. Microw. Wireless Technol., vol. 4, no. 3, pp. 387–397, Apr. 2012.

[5] A. Benvegnú et al., "On-wafer single-pulse thermal load-pull RF characterization of trapping phenomena in AlGaN/GaN HEMTs," IEEE Trans. Microw. Theory Techn., vol. 64, no. 3, pp. 767–775, Mar. 2016.

[6] J. Delprato, D. Barataud, M. Campovecchio, G. Neveux, C. Tolant, and P. Eudeline, "Measured and simulated impact of irregular radar pulse trains on the pulse-to-pulse stability of microwave power amplifiers," IEEE Trans. Microw. Theory Techn., vol. 62, no. 12, pp. 3538–3548, Dec. 2014.

[7] O. Axelsson, N. Billström, N. Rorsman, and M. Thorsell, "Impact of trapping effects on the recovery time of GaN based low noise amplifiers," IEEE Microw. Wireless Compon. Lett., vol. 26, no. 1, pp. 31–33, Jan. 2016.

[8] S. C. Binari et al., "Trapping effects and microwave power performance in AlGaN/GaN HEMTs," IEEE Trans. Electron Devices, vol. 48, no. 3, pp. 465–471, Mar. 2001.

[9] A. Santarelli et al., "Multi-bias nonlinear characterization of GaN FET trapping effects through a multiple pulse time domain network analyzer," in Proc. 10th Eur. Microw. Int. Circuits Conf. (EuMIC), Sep. 2015, pp. 81–84.

[10] J. Delprato et al., "Pulsed gate bias control of GaN HEMTs to improve pulse-to-pulse stability in radar applications," Electron. Lett., vol. 51, no. 13, pp. 1023–1025, Jun. 2015.

[11] J. Xu, R. Jones, S. A. Harris, T. Nielsen, and D. E. Root, "Dynamic FET model-DynaFET-for GaN transistors from NVNA active source injection measurements," in IEEE MTT-S Int. Microw. Symp. Dig., Jun. 2014, pp. 1–3.

[12] C. Chang, V. Di Giacomo-Brunel, D. Floriot, J. Grünenpütt, M. Hosch, and H. Blanck, "Nonlinear transistor modeling for industrial 0.25-μm AlGaN-GaN HEMTs," in *Proc. Eur. Microw. Int. Circuits Conf. (EuMIC)*, Oct. 2013, pp. 500–503.

[13] A. Santarelli *et al.*, "GaN FET nonlinear modeling based on double pulse I/V characteristics," *IEEE Trans. Microw. Theory Techn.*, vol. 62, no. 12, pp. 3262–3273, Dec. 2014.

[14] A. Raffo, G. Bosi, V. Vadalà, and G. Vannini, "Behavioral modeling of GaN FETs: A load-line approach," *IEEE Trans. Microw. Theory Techn.*, vol. 62, no. 1, pp. 73–82, Jan. 2014.

[15] C. Florian, T. Cappello, D. Niessen, R. P. Paganelli, S. Schafer, and Z. Popović, "Efficient programmable pulse shaping for *X*-band GaN MMIC radar power amplifiers," *IEEE Trans. Microw. Theory Techn.*, vol. 65, no. 3, pp. 881–891, Mar. 2017.

[16] M. Roberg, M. Rodriguez, D. Maksimovic, and Z. Popović, "Efficient and linear amplification of spectrally confined pulsed AM radar signals," *IEEE Microw. Wireless Compon. Lett.*, vol. 22, no. 6, pp. 279–281, Jun. 2012.

[17] M. Rodriguez, M. Roberg, A. Zai, E. Alarcon, Z. Popović, and D. Maksimovic, "Resonant pulse-shaping power supply for radar transmitters," *IEEE Trans. Power Electron.*, vol. 29, no. 2, pp. 707–718, Feb. 2014.

[18] A. Zai, M. Pinto, M. Coffey, and Z. Popović, "Supply-modulated radar transmitters with amplitude-modulated pulses," *IEEE Trans. Microw. Theory Techn.*, vol. 63, no. 9, pp. 2953–2964, Sep. 2015.

[19] C. Florian, D. Niessen, T. Cappello, A. Santarelli, F. Filicori, and, Z. Popović, "Pre-pulsing characterization of GaN PAs with dynamic supply," in *IEEE MTT-S Int. Microw. Symp. Dig.*, San Francisco, CA, USA, May 2016, pp. 1–4.

[20] *The NI Vector Signal Transceiver Hardware Architecture*, accessed on Jul. 11, 2017. [Online]. Available: http://www.ni.com/product-documentation/14028/en/

[21] C. Florian, T. Cappello, R. P. Paganelli, D. Niessen, and F. Filicori, "Envelope tracking of an RF high power amplifier with an 8-level digitally controlled GaN-on-Si supply modulator," *IEEE Trans. Microw. Theory Techn.*, vol. 63, no. 8, pp. 2589–2602, Aug. 2015.

[22] A. Zai, L. Dongxue, S. Schafer, and Z. Popović, "High-efficiency *X*-band MMIC GaN power amplifiers with supply modulation," in *IEEE MTT-S Int. Microw. Symp. Dig.*, Jun. 2014, pp. 1–4.

[23] J. C. Pedro, L. C. Nunes, and P. M. Cabral, "Soft compression and the origins of nonlinear behavior of GaN HEMTs," in *Proc. 9th Eur. Microw. Integr. Circuit Conf.*, Rome, Italy, Oct. 2014, pp. 353–356.

[24] C. Florian, R. Cignani, D. Niessen, and A. Santarelli, "A C-band AlGaN-GaN MMIC HPA for SAR," *IEEE Microw. Wireless Compon. Lett.*, vol. 22, no. 9, pp. 471–473, Sep. 2012.

[25] C. Florian, R. Cignani, A. Santarelli, and F. Filicori, "Design of 40-W AlGaN/GaN MMIC high power amplifiers for *C*-band SAR applications," *IEEE Trans. Microw. Theory Techn.*, vol. 61, no. 12, pp. 4492–4504, Dec. 2013.

[26] J. C. Pedro, M. Cabral, T. R. Cunha, and P. M. Lavrador, "A multiple time-scale power amplifier behavioral model for linearity and efficiency calculations," *IEEE Trans. Microw. Theory Techn.*, vol. 61, no. 1, pp. 606–615, Jan. 2013.

[27] G. P. Gibiino, G. Avolio, D. M. M.-P. Schreurs, A. Santarelli, and F. Filicori, "A three-port nonlinear dynamic behavioral model for supply-modulated RF PAs," *IEEE Trans. Microw. Theory Techn.*, vol. 64, no. 1, pp. 133–147, Jan. 2016.

Tommaso Cappello (S'13–M'17) received the M.S. degree in electrical engineering and Ph.D. degree from the University of Bologna, Bologna, Italy, in 2013 and in 2017, respectively.

Since 2017, he has been with the Microwave and RF Research Group, University of Colorado Boulder, Boulder, CO, USA. His current research interests include power electronics, RF electronics, and digital signal processing techniques for high-frequency transmitter applications.

Alberto Santarelli (M'96) received the Laurea degree (*cum laude*) in electronic engineering and Ph.D. degree in electronics and computer science from the University of Bologna, Bologna, Italy, in 1991 and 1996, respectively.

From 1996 to 2001, he was a Research Assistant with the Research Center for Computer Science and Communication Systems, Italian National Research Council, Bologna. In 2001, he joined the Department of Electrical, Electronic and Information Engineering "Guglielmo Marconi," University of Bologna, where he is currently an Associate Professor. He was a Lecturer of applied electronics, high-frequency electronics, and power electronics. His current research interests include the nonlinear characterization and modeling of electron devices and the nonlinear microwave circuit design.

Prof. Santarelli is a member of the European Microwave Association and the Italian Association of Electrical, Electronics, Automation, Information and Communication Technology.

Daniel Niessen (S'05–M'13) received the Ph.D. degree in electronics, computer science and telecommunications from the University of Bologna, Bologna, Italy, in 2013.

From 2013 to 2016, he was a Research Fellow with the Department of Electrical, Electronic and Information Engineering, University of Bologna. His current research interests include the nonlinear characterization and modeling of electron devices and systems and the MMIC design and linearization techniques.

Fabio Filicori was born in Imola, Italy, in 1949. He received the M.S. degree in electronic engineering from the University of Bologna, Bologna, Italy, in 1974.

In 1974, he joined the Department of Electronics, Computer Science and Systems, University of Bologna, initially as a Research Assistant, and then became an Associate Professor of applied electronics. In 1990, he became a Full Professor of applied electronics with the University of Perugia, Perugia, Italy. In 1991, he joined the Faculty of Engineering, University of Ferrara, Ferrara, Italy, where he was a Full Professor responsible for the degree course in electronic engineering. In 1993, he joined the Faculty of Engineering, University of Bologna, as a Full Professor. During his academic career, he has held courses on computer-aided circuit design, electron devices and circuits, and power electronics. His current research interests include the computer-aided design techniques for nonlinear microwave circuits, electron device nonlinear modeling, sampling instrumentation, and power electronics.

Corrado Florian (S'02–M'04) received the Ph.D. degree in electronics from the University of Bologna, Bologna, Italy, in 2004.

Since 2006, he has been a Research Associate with the Department of Electrical, Electronic and Information Engineering, University of Bologna. He is currently a Lecturer of power electronics and RF electronics courses with the University of Bologna. His current research interests include RF and microwave circuit, power electronics, and microwave and power device characterization and modeling.

Zoya Popović (S'86–M'90–SM'99–F'02) received the Dipl.Ing. degree from the University of Belgrade, Belgrade, Serbia, in 1985, and the Ph.D. degree from the California Institute of Technology, Pasadena, CA, USA, in 1990.

Since 1990, she has been with the University of Colorado Boulder, Boulder, CO, USA, where she is currently a Distinguished Professor and holds the Hudson Moore Jr. Endowed Chair with the Department of Electrical, Computer and Energy Engineering. She was named the 2015 Distinguished Research Lecturer of the University of Colorado. In 2001and 2003 and 2014, she was a Visiting Professor with the Technical University of Munich, Munich, Germany, and with ISAE, Toulouse, France, respectively. Since 1991, she has graduated 56 Ph.D. students and currently leads a group of 16 doctoral students and two Post-Doctoral Fellows. Her current research interests include high-efficiency transmitters for radar and communication, low-noise and broadband microwave and millimeter-wave circuits, antenna arrays, wireless powering for batteryless sensors, and medical applications of microwaves such as core-body thermometry and traveling-wave MRI.

Prof. Popović was a recipient of the 1993 and 2006 IEEE MTT-S Microwave Prizes for best journal papers, the 1996 URSI Issac Koga Gold Medal and was named an NSF White House Presidential Faculty Fellow in 1993, the 2000 Humboldt Research Award for Senior U.S. Scientists from the German Alexander von Humboldt Stiftung, and the 2001 Hewlett-Packard/American Society for Engineering Education Terman Medal for combined teaching and research excellence. She was elected a Foreign Member of the Serbian Academy of Sciences and Arts in 2006. In 2013, she was named the IEEE MTT-S Distinguished Educator.